WEP Warwick Evans Publishing

International Journal of Mechanical and Electrical Engineering

ISSN: 3005-9615 (Print), ISSN: 3005-7132 (Online) | Volume 7, Number 3, Year 2025
DOI: https://doi.org/10.62051/ijmee.v7n3.11
Journal homepage: https://wepub.org/index.php/IJMEE/index

# Analysis and Optimization of Hollow Permanent Magnet Motor Performance and Demagnetization in Intelligent Well Electric Control Sliding Sleeve

Yan Zheng [1], Junyu Zhong [1], Xiao Wang [2], Long Wang [1], Zhiqiang Dun [1], Chuanqing Ma [1], Yaowei Shi [1]

[1] School of Mechatronic Engineering, Southwest Petroleum University, Chengdu, Sichuan, China
[2] CNOOC Energy Development Co., Ltd. Engineering Technology Branch, Beijing, China

## ABSTRACT

High temperatures underground can cause demagnetization in the hollow permanent magnet motor of the intelligent well electric control sliding sleeve, affecting the motor's output performance. To address this issue, this paper establishes a finite element simulation model for the motor and, through comparative analysis, selects the outer rotor type hollow permanent magnet motor solution. Environmental temperature and motor structure are the main factors affecting the performance and demagnetization of the intelligent well electric control sliding sleeve permanent magnet motor. Using Taguchi methods and simulation experimental data, the motor structure is optimized. The optimized motor parameter combination is a slot opening width of 2mm, an air gap of 0.3mm, a pole arc coefficient of 0.76, and a permanent magnet thickness of 3.1mm. After optimization, the motor torque increased by 17.219%, the cogging torque decreased by 27.521%, the demagnetization rate decreased by 55.223%, and the efficiency decreased by only 0.149%. After optimization, the torque difference of the motor increased, the motor's working capacity improved, the torque ripple rate also increased, and its stability decreased slightly, but still within an acceptable range.

## KEYWORDS

Intelligent Well Electric Control Sliding Sleeve; Outer Rotor; Permanent Magnet Motor; Motor Performance; Demagnetization Analysis.

## 1. INTRODUCTION

The downhole flow control system is a crucial part of the intelligent well. It can real-time adjust the pressure, fluid flow rate, and wellbore inflow performance of each downhole production layer, realizing multi-layer commingled production, real-time reservoir control and optimized recovery, controlling water coning and gas coning, and accelerating production[1-3].The downhole electric control sliding sleeve is a core component of the electric control flow control system. It can steplessly adjust the opening degree of the throttle port of the electric control sliding sleeve, thereby realizing the dynamic control of the flow rate of each production layer in the oil reservoir[4-5].The power of the electric control sliding sleeve is provided by a motor, which is required to have characteristics such as a simple structure, small size, and high efficiency. The permanent magnet synchronous motor, which boasts advantages including compact structure, reliable operation, high power density, and high efficiency, can be applied in the downhole electric control sliding sleeve[6].As the well depth increases, the operating environment temperature of the motor in the downhole electric control sliding sleeve also rises accordingly. High temperatures can cause demagnetization of the permanent magnet

materials in the motor, which will reduce the motor's output performance and load-carrying capacity[7-9].Therefore, researching the performance, demagnetization analysis, and optimization of the permanent magnet motor for the electric control sliding sleeve in intelligent wells holds significant practical engineering significance for the efficient development of downhole electric control sliding sleeves.

In recent years, scholars at home and abroad have all conducted analysis and optimization on the performance and demagnetization phenomenon of permanent magnet motors. Chen Yunyun [10] proposed a rare-earth-saving permanent magnet synchronous motor with an alternating-pole structure combined with a local Halbach array, using a hybrid permanent magnet material composed of neodymium-iron-boron (NdFeB) and ferrite. A finite element model for local demagnetization of this motor was established, and the anti-demagnetization optimization design of the motor was carried out with the optimization objectives of improving motor performance and reducing the demagnetization rate.Shi Cenwei [6] focused on the local demagnetization fault of permanent magnet synchronous motors, introduced a parameter representing the spatial angle of the demagnetization region, derived the Fourier coefficients of the radial and tangential components of the residual magnetization intensity, and established an analytical model of the motor under the condition of local demagnetization of permanent magnets.

Hu Kun [11] analyzed the demagnetization mechanism of permanent magnets. Taking a surface-mounted permanent magnet synchronous motor as an example, he conducted a comparative analysis of its uniform demagnetization and local demagnetization, and obtained the variation laws of corresponding physical quantities and the diagnostic method for demagnetization faults.Zhang Jidi [12] took the output torque and air-gap magnetic flux density of the permanent magnet synchronous motorized spindle as optimization objectives, established a multi-objective optimization model, determined the optimal material, operating temperature, and optimal fillet radius of the permanent magnet, and proposed several anti-demagnetization measures.Sung G L [13] analyzed the edge effect in the demagnetization analysis of permanent magnet synchronous motors and proposed a simplified yz-plane model that can take the edge effect into account. This model introduces a correction factor based on the traditional 2D finite element analysis of the xy-plane, which effectively improves the analysis accuracy. Finally, this method was applied to conventional motors, and its effectiveness was verified.Ki-Chan K [14] established equivalent magnetic circuit models for three rotor types: single-layer, V-type, and double-layer. A demagnetization analysis method related to the lumped parameters of the magnetic circuit was adopted, an initial design method for the thickness of permanent magnets was proposed, and the finite element method was used to analyze the internal demagnetization distribution of permanent magnets to verify the calculation results of the equivalent magnetic circuit model.Manel K [15] proposed a two-step analysis method to handle both uniform demagnetization and local demagnetization problems simultaneously. This two-step analysis method can clearly distinguish and characterize demagnetization phenomena under certain working conditions (local demagnetization causes specific sub-harmonics), while uniform demagnetization leads to an increase in current amplitude under a given torque.Mariusz B [16] proposed a field model for the electromagnetic-thermal coupling phenomenon in permanent magnet synchronous motors. This model considers the nonlinearity of the magnetic circuit and the influence of temperature on the magnetic, electrical, and thermal properties of materials. Based on this model, an algorithm was further developed to analyze the influence of temperature and the partial demagnetization process of magnets on the operation of self-starting permanent magnet synchronous motors.At present, there are few studies on the performance, demagnetization analysis, and optimization of permanent magnet motors in high-temperature environments; most existing studies focus on the performance and demagnetization phenomena of permanent magnet motors under factors such as overload, overcurrent, and mechanical vibration. Taking the permanent magnet synchronous motor for the electric control sliding sleeve of intelligent wells as the research object, this paper establishes a finite element model of the motor, conducts a comparative analysis of the electromagnetic performance of internal-rotor and external-rotor permanent magnet synchronous motors, and carries out the structural optimization

design of the motor with the optimization objectives of improving motor performance and reducing the motor demagnetization rate. This ensures that the sliding sleeve works safely, reliably, and efficiently under high-temperature operating conditions, and provides technical support for the design and engineering application of downhole intelligent tools.

## 2. STRUCTURE OF PERMANENT MAGNET SYNCHRONOUS MOTOR

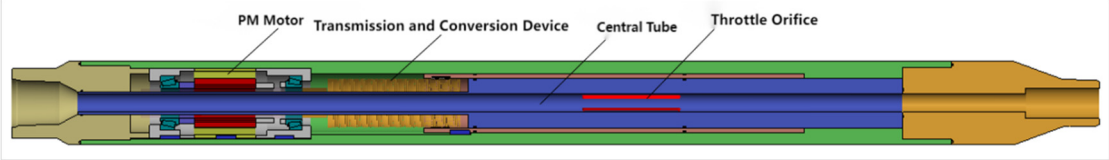


**Fig 1.** Intelligent well electric control sliding sleeve structural scheme

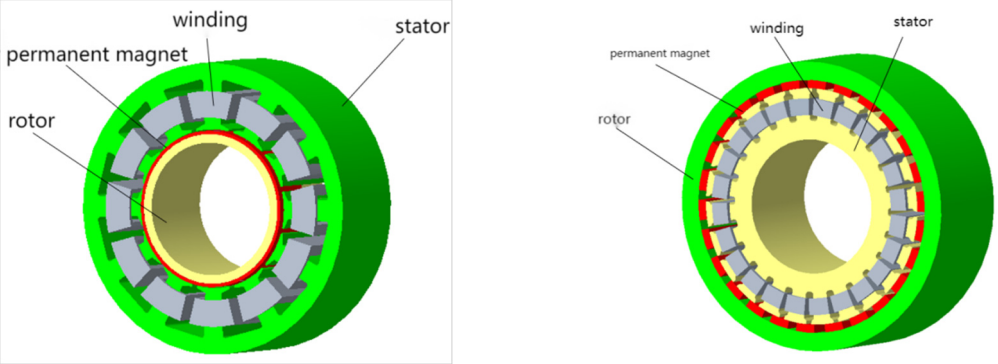


(a)internalinternal-rotor type (b)external-rotor type

**Fig 2.** Structural diagram of the internal motor of the electronically controlled sliding sleeve

The permanent magnet synchronous motor for the electric control sliding sleeve of intelligent wells can be of internal-rotor or external-rotor type. The motor is placed inside the sliding sleeve, and the motor rotor drives the central tube to move axially through a transmission conversion device, thereby realizing stepless flow regulation of downhole production layers. Due to the technological requirements of oil and gas exploitation and the particularity of downhole operations, the motor inside the sliding sleeve adopts a hollow structure. The structural scheme of the electric control sliding sleeve for intelligent wells is shown in Figure 1.

The structure of the permanent magnet synchronous motor inside the electric control sliding sleeve is shown in Figure 2. The internal-rotor permanent magnet motor adopts a 14-pole, 12-slot double-layer winding, with permanent magnets surface-mounted on the outside of the rotor, featuring a compact rotor structure. The external part of the external-rotor permanent magnet motor is composed of a rotor core and permanent magnets, with 26 permanent magnets installed on the inner side of the rotor core; the internal part consists of a stator core and windings, with 24 slots between the teeth. Both the internal-rotor and external-rotor permanent magnet synchronous motors use neodymium-iron-boron N38UH permanent magnet material, which has high coercivity, excellent high-temperature resistance, and relatively good mechanical properties.

# 3. ANALYSIS OF ELECTROMAGNETIC PERFORMANCE OF PERMANENT MAGNET MOTORS

Under the constraint conditions of the same rated power, rated voltage, and motor dimensions (outer diameter ≤ 110mm, inner diameter ≥ 50mm), the electromagnetic performance of the two permanent magnet motors at 20℃ is analyzed and compared. The main parameters of the two motors are shown in Table 1.

## 3.1. Analysis of No-Load Characteristics

The no-load back electromotive force (back-EMF) of a permanent magnet synchronous motor is a crucial parameter, as it directly affects the motor's operating performance. Figure 3 shows the no-load back-EMF waveforms of the internal-rotor and external-rotor motors, while Figure 4 presents a comparison of their harmonic contents.It can be seen from Figure 3 that the amplitude of the back-EMF of the external-rotor motor is higher than that of the internal-rotor motor. From Figure 4, it is observed that the fundamental wave amplitude of the external-rotor motor is greater than that of the internal-rotor motor, and its 3rd harmonic amplitude is significantly lower than that of the internal-rotor motor. Calculations indicate that the back-EMF total harmonic distortion (THD) of the internal-rotor motor is 7.703%, while that of the external-rotor motor is 3.696%. Given that the difference in no-load back-EMF amplitudes between the two motors is not significant, the THD of the external-rotor motor is less than half of that of the internal-rotor motor.

**Table 1.** Main parameters of motor

| **Motor Parameters** | internalinternal-rotor type | external-rotor type |
|---|---|---|
| **Rated Power/w** | 132 | 132 |
| **Rated Voltage/V** | 120 | 120 |
| **Rated Rotational Speed/(r/min)** | 560 | 500 |
| **Number of Pole Pairs** | 7 | 13 |
| **Number of Stator Slot** | 12 | 24 |
| **Stator Outer Diameter/mm** | 110 | 96 |
| **Stator Inner Diameter/mm** | 60 | 50 |
| **Rotor Outer Diameter/mm** | 59 | 108 |
| **Rotor Inner Diameter/mm** | 50 | 97.2 |
| **Permanent Magnet Material** | N38UH | N38UH |

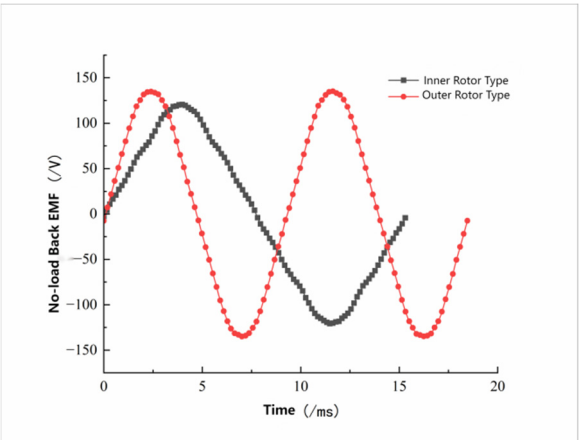


**Fig 3.** No-load BEMF waveform

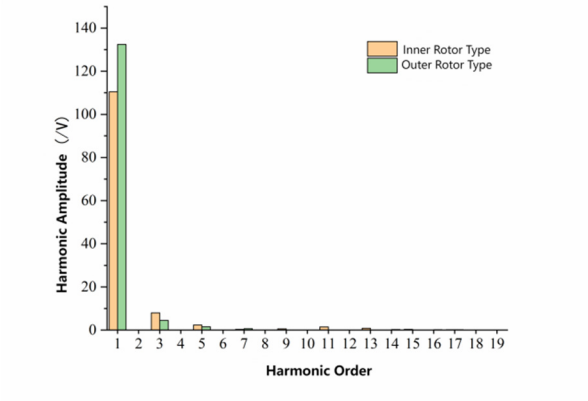


**Fig 4.** Harmonic analysis

### 3.2. Analysis of Torque Characteristics.

The output torque of internal-rotor and external-rotor motors under different input currents at rated speed is analyzed. As shown in Figure 5, when the same current is applied, the output torque of the external-rotor motor is consistently greater than that of the internal-rotor motor. Based on a comparative analysis of the no-load characteristics and torque characteristics of the two motors, the external-rotor permanent magnet synchronous motor is selected as the hollow permanent magnet synchronous motor for the electric control sliding sleeve.

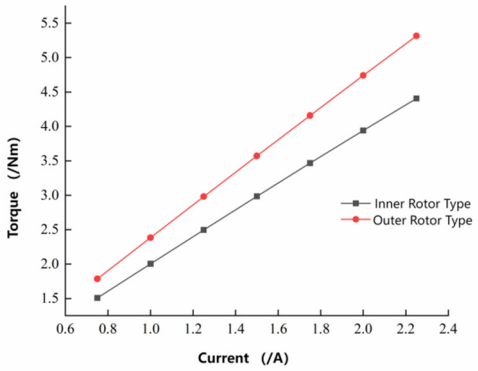


**Fig 5.** Comparison of torque-current characteristics between internal rotor motors and external rotor motors

## 4. SIMULATION ANALYSIS OF THE INFLUENCE OF AMBIENT TEMPERATURE ON MOTOR DEMAGNETIZATION

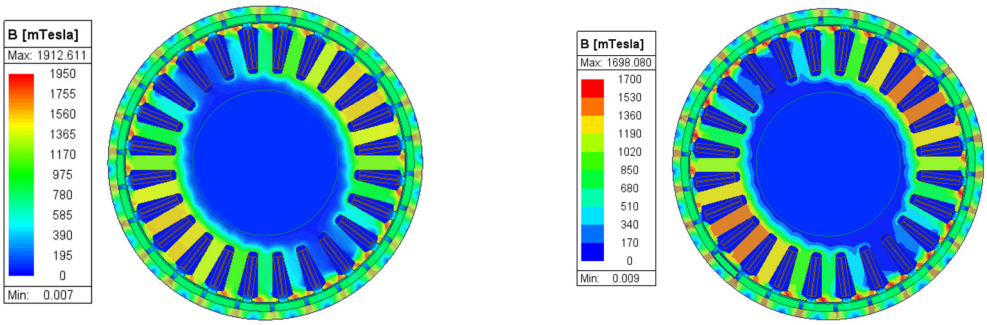


(a) 20℃ (b) 120℃

**Fig 6.** Motor no-load magnetic density contour map

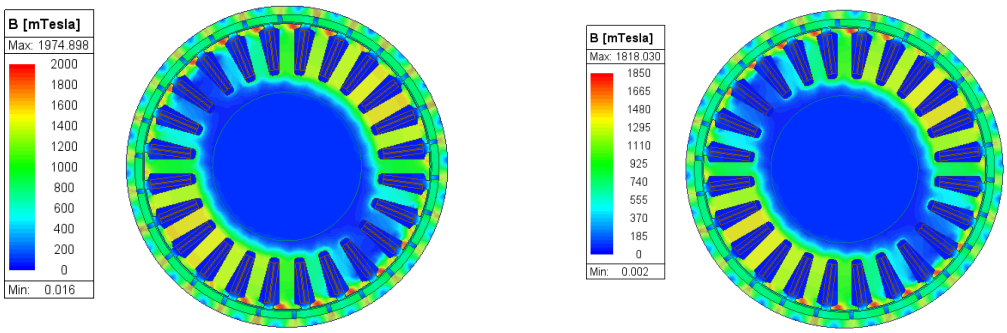


(a) 20°C (b) 120°C

**Fig 7.** Motor load magnetic density contour plot

The motor operates in a high-temperature environment of 120°C for long periods, with low usage frequency, short working duration, and generally constant load. Considering the actual operating conditions, ambient temperature and motor structural design are the main factors affecting the performance and demagnetization of the permanent magnet motor for the electric control sliding sleeve. Electromagnetic simulation software is used to analyze the influence of external ambient temperature on the motor's operation. The external ambient temperature is set to 20°C and 120°C respectively, and simulation analyses of the motor are conducted under these two temperature conditions. The permanent magnet material is set as N38UH, and automatic mesh generation is performed. The no-load and load magnetic flux density nephograms of the motor at 20°C and 120°C are shown in Figures 6 and 7, while the peak values of magnetic induction intensity are listed in Table 2.

**Table 2.** Peak magnetic induction intensity under different ambient temperatures

| Ambient Temperature | Peak Magnetic Induction Intensity | Percentage of Decrease |
|---|---|---|
| 20°C(no-load) | 1912.611 | 0 |
| 120°C(no-load) | 1698.080 | 11.217% (Compared with the no-load condition at 20°C) |
| 20°C(load) | 1974.898 | 0 |
| 120°C(load) | 1818.030 | 7.943% (Compared with the load condition at 20°C) |

It can be seen from Figures 6, 7 and Table 2 that the local stator teeth of the motor are close to magnetic saturation. As the ambient temperature increases, the peak values of no-load and load magnetic induction intensity of the motor decrease. Compared with that at 20°C, the peak no-load magnetic induction intensity of the motor at 120°C decreases by 11.2%, and the peak load magnetic induction intensity at 120°C decreases by 7.9%. The load magnetic induction intensity of the motor's stator teeth at 120°C is basically around 925 mT.

## 5. SIMULATION ANALYSIS ON THE IMPACT OF STRUCTURAL OPTIMIZATION ON MOTOR PERFORMANCE AND DEMAGNETIZATION

On the premise of meeting the design requirements, the motor structure is optimized, and the optimal optimization method is used to find the scheme with the best motor performance and the lowest demagnetization rate. To conveniently represent the average demagnetization degree of the motor, the ratio of the variation of the no-load back electromotive force to the no-load back electromotive force of the motor at 20°C is defined as the average demagnetization rate K of the motor.

$$K = \frac{\Delta E}{E_{20}} \times 100\% \quad (1)$$

In Equation (1), ΔE is the difference between the no-load back electromotive force (back-EMF) of the motor at 20°C and 120°C; $E_{20}$ is the no-load back-EMF of the motor at 20°C.

## 5.1. Taguchi Method for Structural Optimization

**Table 3.** Different impact factors and different level values

| Symbol | Factor Name | Level | | | |
|---|---|---|---|---|---|
| | | 1 | 2 | 3 | 4 |
| A | Slot Opening Width b/mm | 2.9 | 2.6 | 2.3 | 2 |
| B | Air Gap δ/mm | 0.9 | 0.7 | 0.5 | 0.3 |
| C | Pole Arc Coefficient $\alpha_p$ | 0.88 | 0.84 | 0.80 | 0.76 |
| D | Permanent Magnet Thickness $h_m$/mm | 3.1 | 3.2 | 3.3 | 3.4 |

**Table 4.** Orthogonal experimental scheme and simulation experimental data

| Test Number | A | B | C | D | Torque T $T$/(N·m) | Cogging Torque Tcog $T_{cog}$/(mN·m) | Demagnetization Rate $K$/ (%) | Efficiency $\eta$/ (%) |
|---|---|---|---|---|---|---|---|---|
| 1 | 1 | 1 | 1 | 1 | 2.515 | 7.976 | 14.247 | 89.127 |
| 2 | 1 | 2 | 2 | 2 | 2.621 | 8.386 | 12.452 | 88.092 |
| 3 | 1 | 3 | 3 | 3 | 2.735 | 5.316 | 10.692 | 89.115 |
| 4 | 1 | 4 | 4 | 4 | 2.855 | 2.698 | 10.320 | 89.204 |
| 5 | 2 | 1 | 2 | 3 | 2.453 | 2.310 | 15.320 | 89.296 |
| 6 | 2 | 2 | 3 | 4 | 2.559 | 7.000 | 12.923 | 89.299 |
| 7 | 2 | 3 | 4 | 1 | 2.790 | 5.584 | 12.557 | 89.036 |
| 8 | 2 | 4 | 1 | 2 | 2.841 | 9.356 | 8.801 | 88.563 |
| 9 | 3 | 1 | 3 | 4 | 2.410 | 10.764 | 15.064 | 89.445 |
| 10 | 3 | 2 | 4 | 1 | 2.678 | 2.041 | 13.674 | 89.299 |
| 11 | 3 | 3 | 1 | 2 | 2.768 | 5.087 | 9.914 | 88.726 |
| 12 | 3 | 4 | 2 | 3 | 2.866 | 1.227 | 9.095 | 88.734 |
| 13 | 4 | 1 | 4 | 2 | 2.496 | 5.850 | 13.944 | 89.442 |
| 14 | 4 | 2 | 1 | 3 | 2.640 | 17.984 | 11.786 | 88.929 |
| 15 | 4 | 3 | 2 | 4 | 2.743 | 2.207 | 9.315 | 88.914 |
| 16 | 4 | 4 | 3 | 1 | 2.925 | 12.750 | 9.267 | 88.897 |

Four electromagnetic structural parameters of the motor—slot opening width, permanent magnet thickness, air gap length, and pole arc coefficient—are selected as influencing factors, with rated torque, cogging torque, demagnetization rate, and motor efficiency as optimization objectives for optimization. Based on the parametric analysis of the motor, four levels are selected, and the values of different influencing factors at different levels are shown in Table 3. According to the Taguchi

method and simulation analysis, the orthogonal experimental schemes and corresponding finite element simulation data (at 20°C) are obtained, as shown in Table 4.

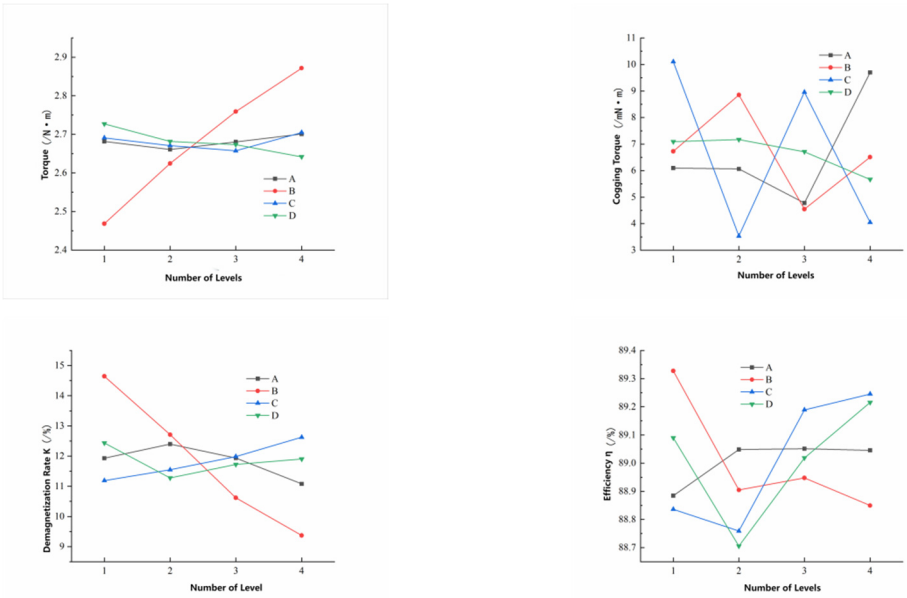


**Fig 8.** Performance effect diagram of each target

**Table 5.** Optimal combination of motor parameters

| Combination | Torque T<br>$T$/(N·m) | Cogging Torque Tcog<br>$T_{cog}$/(mN·m) | Demagnetization Rate<br>$K$/(%) | Efficiency<br>$\eta$/(%) |
|---|---|---|---|---|
| A4, B4, C4, D1 | 2.934 | 5.915 | 10.667% | 89.102% |
| A3, B3, C2, D4 | 2.729 | 4.320 | 10.307% | 88.936% |
| A4, B4, C1, D2 | 2.864 | 4.094 | 8.512% | 88.532% |
| A3, B1, C4, D4 | 2.390 | 8.117 | 14.881% | 89.575% |

**Table 6.** Variance values and proportions of different parameters on various performance indicators of the motor

| Factor | Torque T<br>$T$/(N·m) | | Cogging Torque Tcog<br>$T_{cog}$/(mN·m) | | Demagnetization Rate<br>$K$/(%) | | Efficiency<br>$\eta$/(%) | |
|---|---|---|---|---|---|---|---|---|
| | Variance | Proportion | Variance | Proportion | Variance | Proportion | Variance | Proportion |
| Slot Opening Width | $2.026\times10^{-4}$ | 0.838% | 3.360 | 23.209% | 0.228 | 4.810% | $5.037\times10^{-3}$ | 4.168% |
| Air Gap | $2.270\times10^{-2}$ | 93.942% | 2.324 | 16.049% | 4.051 | 85.491% | $3.537\times10^{-2}$ | 29.271% |
| Pole Arc Coefficient | $3.333\times10^{-4}$ | 1.379% | 8.437 | 58.271% | 0.287 | 6.061% | $4.514\times10^{-2}$ | 37.350% |
| Permanent Magnet Thickness | $9.283\times10^{-4}$ | 3.841% | 0.358 | 2.471% | 0.172 | 3.638% | $3.530\times10^{-2}$ | 29.211% |

The average values of the simulation results under different levels for each parameter are calculated to obtain the effect diagrams of different motor parameters on various performance indicators, as shown in Figure 8. Then, the motor parameters are classified to get the optimal combinations, as listed in Table 5. The variance values of different simulation results under various motor parameters are calculated to analyze the influence proportion of each parameter, as presented in Table 6. Among the four optimal combinations in Table 5, the combination A4B4C4D1 is selected based on the requirement of giving priority to improving motor torque and reducing demagnetization rate.

## 5.2. Simulation Comparative Analysis

The optimized motor parameter combination is as follows: slot opening width of 2 mm, air gap of 0.3 mm, pole arc coefficient of 0.76, and permanent magnet thickness of 3.1 mm. The motor performance (at 20°C) and demagnetization rate (at 120°C) before and after optimization obtained through simulation analysis are shown in Table 7. At an ambient temperature of 120°C, the torque difference and torque ripple rate of the motor before and after optimization are listed in Table 8. After optimization, the motor torque is increased by 17.219%, the cogging torque is reduced by 27.521%, and the efficiency is only decreased by 0.149%. At 120°C, the demagnetization rate of the optimized motor is reduced by 55.223%, the torque difference is increased (indicating improved working capacity of the motor), and the torque ripple rate is also increased. Meanwhile, its stability is somewhat reduced, but it still remains within the allowable range.

**Table 7.** Comparison of motor performance and demagnetization rate before and after optimization

| | Torque T<br>$T$/(N·m) | Cogging Torque Tcog<br>$T_{cog}$/(mN·m) | Demagnetization Rate<br>$K$/(%) | Efficiency<br>$\eta$/(%) |
|---|---|---|---|---|
| Before Optimization | 2.503 | 8.161 | 23.407 | 89.235 |
| After Optimization | 2.934 | 5.915 | 10.667% | 89.102% |

**Table 8.** Motor torque difference and torque ripple rate before and after optimization

| Working Condition | Torque Difference/(N·m) | Torque Ripple Rate |
|---|---|---|
| 120°C(Before Optimization) | 0.060 | 0.024 |
| 120°C(After Optimization) | 0.181 | 0.062 |

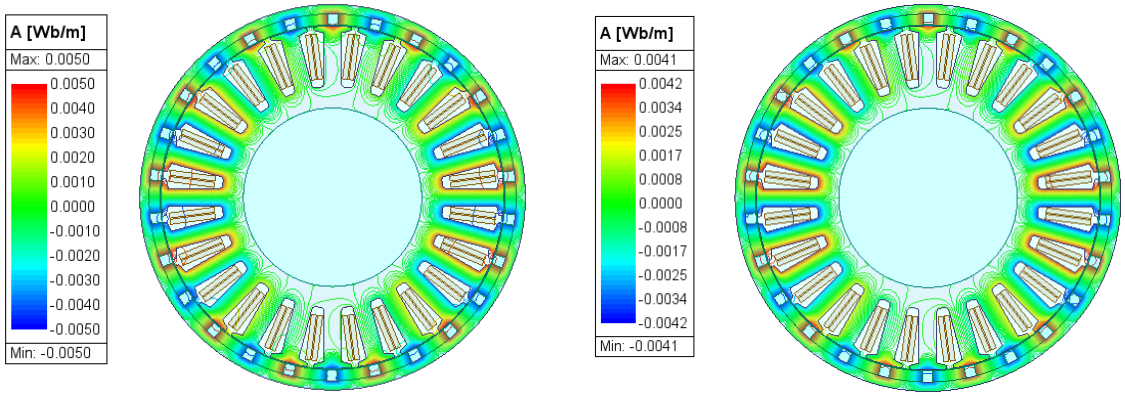


(a) 20°C (b) 120°C

**Fig 9.** Optimized no-load magnetic line diagram of motor

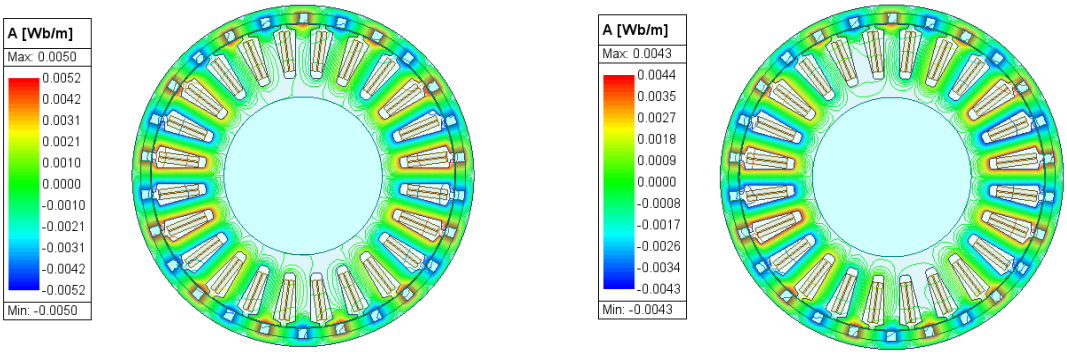


(a) 20℃ (b) 120℃

**Fig 10.** Optimized motor load magnetic line diagram

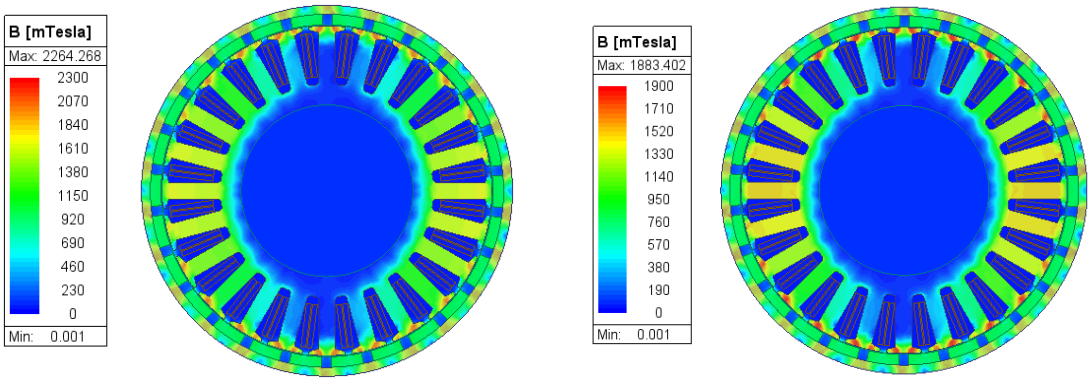


(a) 20℃ (b) 120℃

**Fig 11.** Optimized motor no-load magnetic density cloud map

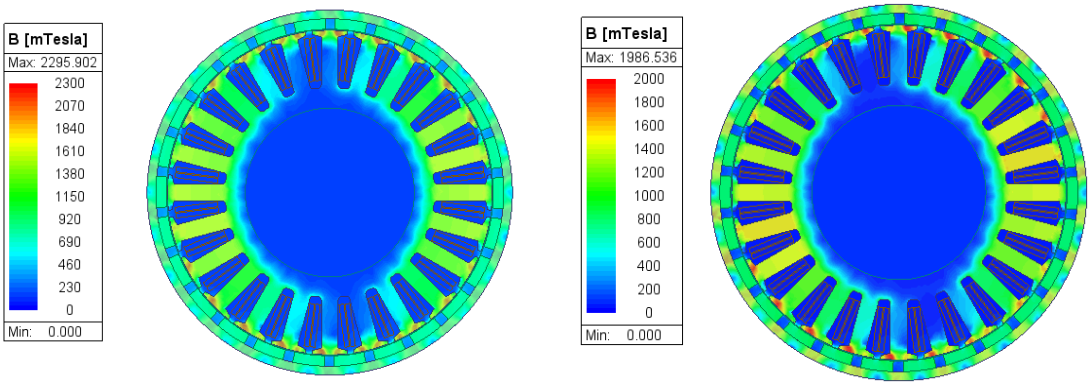


(a) 20℃ (b) 120℃

**Fig 12.** Optimized motor no-load magnetic density cloud map

The no-load and load magnetic flux line diagrams of the optimized motor are shown in Figures 9 and 10, and the no-load and load magnetic flux density nephograms are shown in Figures 11 and 12. It can be seen from Figures 9 and 10 that the overall flux lines are generally evenly distributed, with only a small amount of magnetic leakage existing on the surface of the stator teeth corresponding to the gaps between permanent magnets. Therefore, in the magnetic flux density nephograms of Figures 11 and 12, the magnetic leakage areas show relatively high flux density. At 20°C and 120°C, both under no-load and load conditions, the magnetic flux density on both sides of the stator slot opening is relatively high. Under the load condition at 120°C, the local maximum magnetic flux density

reaches approximately 1.99 T, while the magnetic flux density in the tooth part is below 1.8 T and that in the yoke part is below 1.4 T, which meets the motor design requirements.

## 6. CONCLUSION

(1) Taking the permanent magnet synchronous motor for intelligent well electric control sliding sleeves as the research object, a finite element model of the motor is established. Under the constraints of the same rated power, rated voltage, and motor dimensions, the no-load characteristics and torque characteristics of external-rotor and internal-rotor motors are compared and analyzed, and the external-rotor hollow permanent magnet synchronous motor scheme is selected.

(2) Ambient temperature and motor structure are the main factors affecting the performance and demagnetization of the sliding sleeve permanent magnet motor. Simulation analyses of the external-rotor motor are conducted at ambient temperatures of 20°C and 120°C. The local stator teeth of the motor are close to magnetic saturation, and as the ambient temperature increases, the peak values of no-load and load magnetic induction intensity decrease. Compared with that at 20°C, the peak no-load magnetic induction intensity at 120°C decreases by 11.2%, and the peak load magnetic induction intensity at 120°C decreases by 7.9%.

(3) The Taguchi method and simulation experiment data are used for the structural optimization design of the motor. After optimization, the motor torque is increased by 17.219%, the cogging torque is reduced by 27.521%, and the efficiency is only decreased by 0.149%. At an ambient temperature of 120°C, the demagnetization rate of the optimized motor is reduced by 55.223%, the torque difference is increased (improving the motor's working capacity), and the torque ripple rate is also increased, with its stability slightly reduced but still within the allowable range. At 20°C and 120°C, both under no-load and load conditions, the magnetic flux density on both sides of the stator slot opening is relatively high. Under the load condition at 120°C, the local maximum magnetic flux density reaches approximately 1.99 T, while the magnetic flux density in the tooth part is below 1.8 T and that in the yoke part is below 1.4 T, which meets the motor design requirements.

## ACKNOWLEDGMENTS

Fund Project: CNOOC (China) Limited Beijing Research Center Project "Design and Modular Processing, Integration, and Testing of Downhole Flow Control Systems" (CCL2021R CPS 0399RCN).

## REFERENCES

[1] GUO M L, LI J, YUAN Y L, et al. Hydraulic control intelligent separate zone production technology and its application in Bohai oilfield[J]. China Petroleum Machinery, 2023, 51(11): 138-143.

[2] SONG J X, ZHOU L C, WANG Y L, et al. Design of wireless power transmission system applied to full electric control intelligent wells[J]. China Petroleum Machinery, 2025, 53(1): 28-36.

[3] NAGIB M, EZUKA I, NASR G G. Economic comparison of intelligent wells in simultaneous production of oil and gas reserves from single wellbore[J]. SPE Production and Operations, 2011, 26(2): 203-210.

[4] FENG G C, YIN Y J, MA L S, et al. A discussion on the development and application of intelligent well technology in offshore oilfields[J]. Journal of Southwest Petroleum University (Science & Technology Edition), 2022, 44(4): 153-164.

[5] AN C H, WANG J L. Technical analysis of hydraulic control systems for hydraulically controlled intelligent well completion[J]. Petrochemical Industry Applications, 2024, 43(5): 95-99.

[6] SHI C W, PENG L, ZHANG Z, et al. Modeling and analysis of demagnetization fault in surface-mounted permanent magnet synchronous motors with voltage source excitation[J]. Transactions of China Electrotechnical Society, 2025, 40(8): 2430-2440.

[7] CUI G, XIONG B, HUANG K J, et al. Spatial distribution characteristics and influencing factors of demagnetization in permanent magnet motors for electric vehicles[J]. Transactions of China Electrotechnical Society, 2023, 38(22): 5959-5974.

[8] XIE Y, JIANG J N, CAI W, et al. Demagnetization failure of surface-mounted high-speed permanent magnet synchronous motors and research on local infiltration of heavy rare earths in magnets[J]. Electric Machines and Control, 2024, 28(2): 44-53.

[9] ZHANG D, ZHAO J W, DONG F, et al. Research on partial demagnetization fault diagnosis of permanent magnet synchronous linear motors based on probabilistic neural network algorithm[J]. Proceedings of the CSEE, 2019, 39(1): 296-306, 344.

[10] CHEN Y Y, LI Z J, ZHOU X, et al. Analysis and optimization of anti-demagnetization performance of composite-structured hybrid permanent magnet motors[J]. Electronic Measurement Technology, 2023, 46(11): 1-6.

[11] HU K, SHI X, WANG H D, et al. Analysis and experimental research on demagnetization fault of permanent magnet synchronous motors[J]. Research and Exploration in Laboratory, 2023, 42(11): 106-112.

[12] ZHANG J D, SHAN W T, CHEN K P, et al. Research and optimization of demagnetization performance of permanent magnet synchronous motorized spindles[J]. Machine Tool & Hydraulics, 2025, 53(1): 24-31.

[13] SUNG G L, KWANG-SOO K, JU L, et al. A novel methodology for the demagnetization analysis of surface permanent magnet synchronous motors[J]. IEEE Transactions on Magnetics, 2016, 52(3): 7003404.

[14] KI-CHAN K, KWANGSOO K, HEE J K, et al. Demagnetization analysis of permanent magnets according to rotor types of interior permanent synchronous motor[J]. IEEE Transactions on Magnetics, 2009, 45(6): 2799-2802.

[15] MANEL K, ELHOUSSIN E, NAOUREZ B, et al. Motor current signature analysis-based permanent magnet synchronous motor demagnetization characterization and detection[J]. Machines, 2020, 8(3): 35.

[16] MARIUSZ B, WOJCIECH S, WIESLAW L. Analysis of the partial demagnetization process of magnets in a line-start permanent magnet synchronous motor[J]. Energies, 2020, 13(21): 5621.